Wave Motion 134 (2025) 103507

Contents lists available at ScienceDirect

Wave Motion

journal homepage: www.elsevier.com/locate/wamot

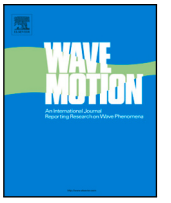

On water hammer waves

Carmine Di Nucci [a,*], Kamil Urbanowicz [b], Simone Michele [c], Daniele Celli [a], Davide Pasquali [a], Marcello Di Risio [a]

[a] Environmental and Maritime Hydraulic Laboratory (LIam), Civil, Construction-Architectural and Environmental Engineering Department (DICEAA), University of L'Aquila, Piazzale Ernesto Pontieri 1, Monteluco di Roio, L'Aquila, 67100, Italy
[b] Faculty of Mechanical Engineering and Mechatronics, West Pomeranian University of Technology, Al. Piastòw 17, Szczecin, 70-310, Poland
[c] Department of Civil Engineering and Computer Science, Università degli Studi di Roma "Tor Vergata", Via del Politecnico 1, Roma, 00133, Italy

ARTICLE INFO

Keywords:
Quasi-incompressible approximation
RANS equations
Entropy production
Linear damped wave equation
Water hammer

ABSTRACT

Water hammer waves, i.e., low-frequency, low-Mach number propagation of finite-amplitude pressure waves in pipe flow, are investigated by means of the wave equation proposed in Di Nucci et al., 2024a, 2024b. The wave equation, resembling a linear damped wave equation, comes from the turbulent-viscosity model based on the quasi-incompressible Reynolds Averaged Navier–Stokes equations. Changes in temperature due to entropy production are neglected, and adiabatic conditions are imposed. Additional insights on the assumptions used to derive the wave equation are also provided. Focusing on the one-dimensional propagation of pressure waves in liquid-filled pipes (without cavitation), analytical solution of the wave equation is tested against experimental data available from the literature. The impact of the simplifying assumptions on the quantitative outcomes appears to be small; therefore a good level of accuracy in replicating water hammer wave characteristics (including damping, smoothing, and maximum pressure peak) is achieved. Results show that the Reynolds number has minimal influence on water hammer wave propagation, i.e., the vorticity field has no remarkable effect on flow behavior. Deeper attention is given to entropy production, and to the role played by the dimensionless number which is identified as predominant in water hammer wave propagation. Damping properties are also determined.

1. Introduction

In fluid mechanics literature, many theories link the longitudinal wave attenuation to both the thermomechanical constitutive equation and the thermodynamic parameters (the readers are referred to [1,2] for details). Under viscous flow regimes, the viscosity effects on wave attenuation in internal flows (pipe flows) are analyzed in [3]. Furthermore, turbulence causes more attenuation than viscosity. According to experimental data, in internal flows the turbulence attenuation is dominant at sufficiently low-frequencies [4]. The attenuation is attributed to turbulent absorption effects in the boundary layer [5]. Within the framework of small amplitude waves, the linearized Navier–Stokes equations are considered [6], and the wall shear stress of the perturbation field is employed to characterize the turbulent effects [7,8]. As the shear stress is independent of the compressibility, the incompressible flow is assumed, and most models are based on extending the standard eddy-viscosity model [9]. Some theoretical modeling, numerical simulations, and comparison with experimental data can be found in [8].

* Corresponding author.
E-mail address: carmine.dinucci@univaq.it (C. Di Nucci).

https://doi.org/10.1016/j.wavemoti.2025.103507
Received 5 August 2024; Received in revised form 12 January 2025; Accepted 26 January 2025
Available online 4 February 2025

In hydraulic applications, the main attention is focused on water hammer waves [10], i.e., low-frequency, low-Mach number propagation of finite-amplitude longitudinal waves (specifically pressure waves) in pipe flow. Water hammer waves, which arise as a result of local velocity variations due to valve maneuvers, play a crucial role in the management of water systems, involving both fluid structure interaction, and pipe diagnostics based on frequency analysis [11–13]. In hydraulic literature (one-dimensional models), the most used approach to evaluate the energy loss that characterizes water hammer waves is the frequency-dependent friction model [14–17]. According to this model, the fluid friction increases as a result of an additional shear stress appearing in the unsteady pipe flow. This model, which replaces the steady friction model based on the Darcy–Weisbach equation with an unsteady friction model [10,18], ignores compressing effects. In contrast, one-dimensional models that incorporate the influence of turbulent compressibility on wave attenuation, regardless of unsteady friction, are proposed in [19–22].

This paper further explores and develops the wave equation model proposed in [21,22]. In model building, adiabatic conditions are imposed, and changes in temperature due to entropy production are assumed to be negligible. Low-frequency limit is adopted, thus the second viscosity is assumed to be independent of the wave frequency [2]; on the other hand, low-Mach number limit enables the quasi-incompressible approximation to derive the Reynolds Averaged Navier–Stokes (RANS) equations. The quasi-incompressible approximation [23] is a good compromise between the incompressible and fully compressible descriptions. If, on the one hand, the incompressible description is not able to describe the compressibility effects, on the other hand, the fully compressible description is too complex for any analytical studies. Water hammer waves involve both shearing processes, measured by vorticity, and compressing processes, measured by dilatation (the velocity field divergence), pressure and other thermodynamic variables, such as entropy. These processes are coupled with each other and with other processes (e.g., turbulent mixing and convective processes) within the flow field and at the solid boundary [24]. In [21,22] it is conjectured that the compressing processes are predominant over the others. In this paper, the dimensional analysis is used to investigate this conjecture. As a result of this procedure, the working hypotheses are highlighted; the model validity range is established; the role of different dimensionless numbers is clarified. The dimensional analysis suggests that, in a short time scale, the Reynolds number has no great influence on the flow behavior, i.e., the vorticity field does not significantly influence the water hammer wave propagation. Additionally, the same analysis identifies a single dimensionless number governing the flow behavior.

To deepen the theoretical aspects, testing and validation of the wave equation model for water hammer waves, an overview is presented in Section 2. The basic hypotheses are introduced; the turbulent-viscosity model, based on the quasi-incompressible RANS equations, is synthesized; the results of the dimensional analysis are discussed; the wave equation is derived. In Section 3, the wave equation, resembling a linear damped wave equation, is used to investigate the one-dimensional water hammer waves in liquid-filled pipes (without cavitation). The analytical solution of the wave equation, obtained under suitable initial and boundary conditions, is tested against literature experimental data. The findings indicate that the wave equation offers a satisfactory representation of water hammer phenomenon for a range of practical cases. The results are discussed, and, among the original aspects, emphasis is placed on entropy production, and, in turn, on the role played by the dimensionless number governing water hammer waves. Deepening insights confirm the minimal influence of Reynolds number on water hammer wave propagation. Additionally a damping analysis is also performed. Section 4 provides a summary of the primary conclusions.

2. 3D water hammer wave equation

2.1. Governing equations

The RANS equations are used to describe the propagation of longitudinal waves in quasi-compressible fluids. Longitudinal waves arise as a consequence of a perturbation of pre-existing thermomechanical fields (such as velocity $\boldsymbol{v}$, pressure p, density ρ) and propagate with the (relative) celerity c (Fig. 1). In the paper, the notation p denotes the relative thermodynamic pressure [25].

For quasi-incompressible Navier–Stokes fluids, the RANS equations read as [19,21,22]:

$$\frac{\partial \rho}{\partial t} + \nabla\rho \cdot [\boldsymbol{v}] + \rho \nabla \cdot [\boldsymbol{v}] = 0, \tag{1}$$

$$\rho \frac{\partial}{\partial t}[\boldsymbol{v}] + \rho \nabla [\boldsymbol{v}] \cdot [\boldsymbol{v}] = -\rho g \hat{\boldsymbol{e}}_z - \nabla \cdot [\underline{\boldsymbol{T}}] - \nabla \cdot \underline{\boldsymbol{T}}_{\mathrm{Re}}, \tag{2}$$

$$\rho = \rho_0 \mathrm{e}^{\frac{p}{\epsilon}}, \tag{3}$$

where g the modulus of the gravitational acceleration; $\hat{\boldsymbol{e}}_z$ the unit vector directed along the vertical direction; $\underline{\boldsymbol{T}}$ the Cauchy stress tensor; $\underline{\boldsymbol{T}}_{\mathrm{Re}}$ the Reynolds stress tensor; ρ_0 the reference density at the reference atmospheric relative pressure $p_0 = 0$; ϵ the bulk modulus of elasticity (with ϵ large in comparison with the occurring pressures). The Reynolds decomposition is expressed as:

$$b = [b] + b', \tag{4}$$

where $[b]$ is the average value of a generic field b, and b' the turbulent fluctuation.

The RANS equations (1)–(3) are obtained by using the Russo Spena model [19], according to which the turbulent fluctuations in fluid density are assumed to be negligible, i.e., $\rho' = 0$; thus, the standard RANS procedure can be applied [26], without invoking the Favre averaging.

It should be noted that, in agreement with the barotopic Eq. (3):

- isothermal conditions are assumed;

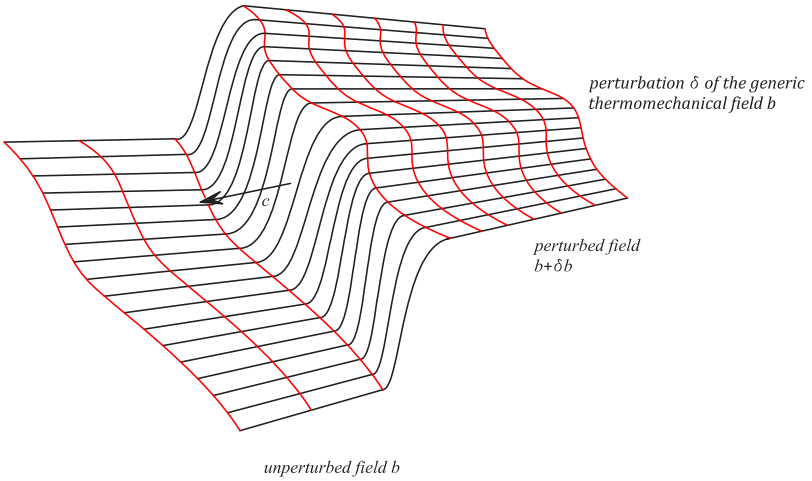

Fig. 1. Sketch of the longitudinal wave propagation.

- ε is pressure independent;
- the celerity c is given as:

$$c = [c] = \sqrt{\frac{\varepsilon}{\rho}}. \tag{5}$$

By combining Eqs. (1) and (3), the continuity equation becomes:

$$\frac{\partial [p]}{\partial t} + \nabla [p] \cdot [\boldsymbol{v}] + \varepsilon \nabla \cdot [\boldsymbol{v}] = 0. \tag{6}$$

The Cauchy stress tensor $\underline{\boldsymbol{T}}$ is decomposed as:

$$\underline{\boldsymbol{T}} = \underline{\boldsymbol{T}}_{vis} + p\underline{\mathbf{1}}, \tag{7}$$

where $\underline{\boldsymbol{T}}_{vis}$ is the viscous stress; $\underline{\mathbf{1}}$ the unit tensor. The constitutive equation reads as [26]:

$$\underline{\boldsymbol{T}}_{vis} = -2\mu_1 \underline{\boldsymbol{D}} - \mu_2 (\nabla \cdot \boldsymbol{v}) \underline{\mathbf{1}}, \tag{8}$$

where $\underline{\boldsymbol{D}}$ is the strain rate tensor $\underline{\boldsymbol{D}} = \frac{1}{2}\left(\nabla \boldsymbol{v} + \nabla \boldsymbol{v}^{\mathrm{T}}\right)$; μ_1 the first viscous coefficient; μ_2 the second viscosity. Consistent with the standard treatment for Navier–Stokes fluids, the viscous coefficients can be assumed as pressure independent [2]. Low-frequency assumption is also introduced, thus the second viscosity can be assumed to be independent of the wave frequency. The dependence of the second viscosity on the frequencies, which can occur at very high-frequencies, is called dispersion [2]. Accordingly, it can be assumed that $\mu_2 = O\left(\mu_1\right)$ [2]. The surface forces are expressed as:

$$-\nabla \cdot \left[\underline{\boldsymbol{T}}\right] = -\nabla [p] + \left(2\mu_1 + \mu_2\right) \nabla (\nabla \cdot [\boldsymbol{v}]) - \mu_1 \nabla \times [\boldsymbol{\omega}], \tag{9}$$

where $\boldsymbol{\omega} = \nabla \times \boldsymbol{v}$ is the vorticity. Hence, the momentum equation (2) reads as:

$$\rho \frac{\partial}{\partial t} [\boldsymbol{v}] + \rho \nabla [\boldsymbol{v}] \cdot [\boldsymbol{v}] = -\rho g \hat{\boldsymbol{e}}_z - \nabla [p] + \left(2\mu_1 + \mu_2\right) \nabla (\nabla \cdot [\boldsymbol{v}]) - \mu_1 \nabla \times [\boldsymbol{\omega}] - \nabla \cdot \underline{\boldsymbol{T}}_{\mathrm{Re}}. \tag{10}$$

In line with Eq. (7), the Reynolds stress tensor is decomposed as [21,22]:

$$\underline{\boldsymbol{T}}_{\mathrm{Re}} = \underline{\boldsymbol{T}}_{tur} + p_{tur} \underline{\mathbf{1}}, \tag{11}$$

where $\underline{\boldsymbol{T}}_{tur}$ is the homologue of $\left[\underline{\boldsymbol{T}}_{vis}\right]$; p_{tur} the homologue of $[p]$ (p_{tur} is referred to as the relative turbulent pressure). In analogy with Eq. (9), the turbulent surface forces can be expressed as:

$$-\nabla \cdot \underline{\boldsymbol{T}}_{\mathrm{Re}} = -\nabla p_{tur} + f_1 (\nabla \cdot [\boldsymbol{v}]) + f_2 ([\boldsymbol{\omega}]), \tag{12}$$

where f_1 is an implicit function of $\nabla \cdot [\boldsymbol{v}]$, f_2 an implicit function of $[\boldsymbol{\omega}]$. The functions f_1 and f_2 can be made explicit by invoking the Boussinesq turbulent-viscosity hypothesis. Following [19], f_1 can be given as:

$$f_1 (\nabla \cdot [\boldsymbol{v}]) = \mu_{d,tur} \nabla (\nabla \cdot [\boldsymbol{v}]), \tag{13}$$

where $\mu_{d,tur}$ is the turbulent dilatational viscosity; following [21,27], f_2 can be expressed as:

$$f_2 ([\boldsymbol{\omega}]) = \mu_{r,tur} \nabla^2 (\nabla \times [\boldsymbol{\omega}]), \tag{14}$$

where $\mu_{r,tur}$ is the turbulent rotational viscosity. The Boussinesq hypothesis leads to assume $p_{tur} = p_{tur}([\boldsymbol{v}])$; following [21,22], ∇p_{tur} can be modeled as:

$$\nabla p_{tur} = \xi_{tur} \nabla \frac{[v]^2}{2}, \tag{15}$$

where ξ_{tur} is a turbulent diffusion coefficient. As shown in [21,22], the term ∇p_{tur} is a convective term that takes into account the effects of turbulent fluctuations on the momentum flux, i.e., the tensor $p_{tur}\underline{\mathbf{1}}$ is not responsible for entropy production. According to Eqs. (13)–(15), the turbulent viscosities and the turbulent diffusion coefficient are assumed to be constant (this is done to simplify the model). Thus, the RANS momentum equation reads as:

$$\begin{aligned} &\rho \frac{\partial}{\partial t}[\boldsymbol{v}] + \rho \nabla [\boldsymbol{v}] \cdot [\boldsymbol{v}] \\ &= -\rho g \hat{\boldsymbol{e}}_z - \nabla [p] - \xi_{tur} \nabla \frac{[v]^2}{2} - \mu_1 \nabla \times [\boldsymbol{\omega}] + \left(2\mu_1 + \mu_2\right) \nabla \left(\nabla \cdot [\boldsymbol{v}]\right) + \mu_{d,tur} \nabla \left(\nabla \cdot [\boldsymbol{v}]\right) + \mu_{r,tur} \nabla^2 \left(\nabla \times [\boldsymbol{\omega}]\right). \end{aligned} \tag{16}$$

2.2. Water hammer wave equation

The different processes involved in water hammer wave propagation, such as compressing, shearing, and convective processes, operate on different time scales. According to the governing equations, both a short time scale $t_S = \frac{L_0}{c_0}$ and a long time scale $t_L = \frac{L_0}{U_0}$ can be defined, where L_0 is the length scale, U_0 the reference value of the velocity, $c_0 = \sqrt{\frac{\varepsilon}{\rho_0}}$ the reference value of the wave celerity. In typical hydraulic systems, $U_0 \ll c_0$ [28]. The choice of the time scale depends on the topics of interest. By focusing on the processes that act on short time scale, the dimensionless form of the system of equations, given by the continuity equation (6), the momentum equation (16), and the barotropic equation (3), reads as (the terms with an overtilde are dimensionless):

$$\frac{1}{\mathrm{Ma}} \frac{\partial [\tilde{p}]}{\partial \tilde{t}} + \tilde{\nabla} [\tilde{p}] \cdot [\tilde{\boldsymbol{v}}] + \frac{1}{\mathrm{Ma}} \tilde{\nabla} \cdot [\tilde{\boldsymbol{v}}] = 0, \tag{17}$$

$$\begin{aligned} &\frac{1}{\mathrm{Ma}} \frac{\partial [\tilde{\boldsymbol{v}}]}{\partial \tilde{t}} + \tilde{\nabla} [\tilde{\boldsymbol{v}}] \cdot [\tilde{\boldsymbol{v}}] \\ &= -\frac{1}{\mathrm{Fr}^2} \hat{\boldsymbol{e}}_z - \frac{1}{\mathrm{Ma}} \frac{1}{\tilde{\rho}} \tilde{\nabla} [\tilde{p}] - \frac{1}{\mathrm{D}_{tur}} \tilde{\rho} \tilde{\nabla} \frac{[\tilde{v}]^2}{2} - \frac{1}{\mathrm{Re}} \frac{1}{\tilde{\rho}} \tilde{\nabla} \times [\tilde{\boldsymbol{\omega}}] + \frac{1}{\mathrm{RS}} \frac{1}{\tilde{\rho}} \tilde{\nabla} \left(\tilde{\nabla} \cdot [\tilde{\boldsymbol{v}}]\right) + \frac{1}{\mathrm{RS}_{tur}} \frac{1}{\tilde{\rho}} \tilde{\nabla} \left(\tilde{\nabla} \cdot [\tilde{\boldsymbol{v}}]\right) + \frac{1}{\mathrm{Re}_{tur}} \frac{1}{\tilde{\rho}} \tilde{\nabla}^2 \left(\tilde{\nabla} \times [\tilde{\boldsymbol{\omega}}]\right), \end{aligned} \tag{18}$$

$$\tilde{\rho} = \mathrm{e}^{\frac{1}{\mathrm{Ma}}[\tilde{p}]}, \tag{19}$$

where:

- $\mathrm{Ma} = \frac{U_0}{c_0}$ is the Mach number;
- $\mathrm{Fr} = \frac{U_0}{\sqrt{g L_0}}$ the Froude number;
- $\mathrm{D}_{tur} = \frac{\rho_0}{\xi_{tur}}$ the turbulent diffusion number;
- $\mathrm{Re} = \frac{\rho_0 U_0 L_0}{\mu_1}$ the Reynolds number;
- $\mathrm{RS} = \frac{p_0 L_0}{(2\mu_1 + \mu_2) c_0}$ the Russo Spena number [10], with $p_0 = \rho_0 c_0 U_0$ the reference value of the pressure (the Joukowsky pressure rise [29]);
- $\mathrm{RS}_{tur} = \frac{p_0 L_0}{\mu_{d,tur} c_0}$ the turbulent Russo Spena number;
- $\mathrm{Re}_{tur} = \frac{\rho_0 U_0 L_0^3}{\mu_{r,tur}}$ the turbulent Reynolds number.

The system of Eqs. (17)–(19) can be reduced to:

$$\frac{\partial [\tilde{p}]}{\partial \tilde{t}} + \tilde{\nabla} \cdot [\tilde{\boldsymbol{v}}] = 0, \tag{20}$$

$$\frac{\partial [\tilde{\boldsymbol{v}}]}{\partial \tilde{t}} = -\tilde{\nabla} [\tilde{p}] + \frac{1}{\Lambda} \tilde{\nabla} \left(\tilde{\nabla} \cdot [\tilde{\boldsymbol{v}}]\right), \tag{21}$$

$$\tilde{\rho} = 1, \tag{22}$$

where:

$$\Lambda = \frac{\mathrm{RS}_{tur}}{\mathrm{Ma}} = \frac{c_0 L_0}{\nu_{d,tur}} \tag{23}$$

is the ratio of inertial forces to turbulent compressible forces, with $\nu_{d,tur} = \frac{\mu_{d,tur}}{\rho_0}$ denoting the kinematic turbulent dilatational viscosity.

One-dimensional form of Eqs. (20), (21) are given in [21,22].

It has to be stressed that Eqs. (20)–(22) have been derived:

- under low-Mach number approximation, $\mathrm{Ma} \ll 1$;

- by conjecturing that
  - ▷ $\frac{\mathrm{Ma}}{\mathrm{D}_{tur}} = \frac{U_0 \xi_{tur}}{c_0 \rho_0} \ll 1$,
  - ▷ $\frac{\mathrm{Ma}}{\mathrm{Re}} = \frac{\mu_1}{c_0 \rho_0 L_0} \ll 1$,
  - ▷ $\frac{\mathrm{Ma}}{\mathrm{RS}} = \frac{U_0 (2\mu_1 + \mu_2)}{p_0 L_0} \ll 1$,
  - ▷ $\frac{\mathrm{Ma}}{\mathrm{Re}_{tur}} = \frac{\mu_{r,tur}}{c_0 \rho_0 L_0^3} \ll 1$;
- by assuming that $\frac{\mathrm{RS}_{tur}}{\mathrm{RS}} = \frac{(2\mu_1 + \mu_2)}{\mu_{d,tur}} \ll 1$;
- by neglecting the effect of gravity (i.e., assuming that the Froude number has a marginal role).

Thus, in the short time scale limit, the convective processes, along with viscous processes and turbulent shearing processes, can be considered as irrelevant (note that as $\mu_2 = O(\mu_1)$, then $\frac{\mathrm{Ma}}{\mathrm{RS}} = O\left(\frac{\mathrm{Ma}}{\mathrm{Re}}\right)$). On the other hand, the assumption $\frac{\mathrm{RS}_{tur}}{\mathrm{RS}} \ll 1$ implies that the wave attenuation is mainly attributed to the turbulent compressing processes. As the density variations can be neglected, the wave celerity is assumed to be constant, $c = c_0$.

The wave equation, obtained from the momentum Eq. (20) and the continuity Eq. (21), is expressed by the linear damped wave equation:

$$\frac{\partial^2 [\tilde{\boldsymbol{v}}]}{\partial \tilde{t}^2} = \tilde{\nabla}\left(\tilde{\nabla} \cdot [\tilde{\boldsymbol{v}}]\right) + \frac{1}{\Lambda} \frac{\partial}{\partial \tilde{t}} \tilde{\nabla}\left(\tilde{\nabla} \cdot [\tilde{\boldsymbol{v}}]\right), \tag{24}$$

or, alternatively, by:

$$\frac{\partial^2 [\tilde{p}]}{\partial \tilde{t}^2} = \tilde{\nabla}^2 [\tilde{p}] + \frac{1}{\Lambda} \tilde{\nabla}^2 \frac{\partial [\tilde{p}]}{\partial \tilde{t}}. \tag{25}$$

Accordingly, in the short time scale limit, Λ is the only dimensionless number governing the water hammer wave propagation. Due to no significant influence of the Reynolds number, the interaction between the water hammer waves and the vorticity field is assumed to be very weak (i.e., this interaction acts on the long time scale). As a result, the turbulent fluctuations, from which turbulent dilatational viscosity arises, are a consequence of the rapid compression and expansion due to the passage of water hammer waves. The Reynolds number appears unsuitable to describe this kind of turbulence transition, which can be related only to the compressing processes. Heuristic considerations on the transition to turbulence due to compressing processes, and on the role played by the Russo Spena number, can be found in [20,21].

The averaged kinetic energy equation, deduced from the inner product of the momentum Eq. (21) with $[\tilde{\boldsymbol{v}}]$, is given as:

$$\frac{\partial}{\partial \tilde{t}} \frac{[\tilde{v}]^2}{2} = -\tilde{\nabla} \cdot ([\tilde{p}]\,[\tilde{\boldsymbol{v}}]) + [\tilde{p}]\,\tilde{\nabla} \cdot [\tilde{\boldsymbol{v}}] + \frac{1}{\Lambda} \tilde{\nabla} \cdot \left(\left(\tilde{\nabla} \cdot [\tilde{\boldsymbol{v}}]\right)[\tilde{\boldsymbol{v}}]\right) - [\tilde{\varphi}], \tag{26}$$

where the averaged dissipation function $[\tilde{\varphi}]$ is given as:

$$[\tilde{\varphi}] = \frac{1}{\Lambda} \left(\tilde{\nabla} \cdot [\tilde{\boldsymbol{v}}]\right)^2. \tag{27}$$

The dissipation function, which provides the rate of dissipation of the kinetic energy, is proportional to the rate of entropy production. According to Eq. (27), the dimensionless number Λ influences the entropy production: the smaller Λ the shorter the time needed for entropy production to reach the asymptotic value given by the initial kinetic energy.

3. Validation

3.1. Test cases

Different sets of experimental data available in the literature [15,30–32] are used to validate the model equations. The test cases refer to water hammer waves in standard reservoir-pipe-valve systems, where a pipe of length L and diameter D connects an upstream pressurized tank to a downstream valve (Fig. 2). In test cases no cavitation phenomena occur (vapor bubbles can play a dominant role in flow behavior [33]). Consideration is given to horizontal (or sub-horizontal) pipes with a constant diameter. Starting from the steady-state flow conditions, water hammer waves arise as a result of local velocity variations due to downstream valve maneuvers (a schematic sketch is presented in Fig. 3). The experimental data concern the pressure time-series recorded in the downstream section of steel pipes.

In [15], the pipe length is $L = 37.23$ m, and the pipe diameter is $D = 0.0221$ m. The closing of the valve (ball valve) is performed by a torsional spring actuator (the closure time may be set from 5 to 10 ms). A piezoelectric pressure transducer is located close to the end of the pipe. The water temperature is continuously monitored and the valve position during closure is measured using optical sensors. Data acquisition and processing are performed using a real-time data acquisition system.

In [30], $L = 177.4$ m, $D = 0.036$ m; in [31], $L = 72$ m, $D = 0.042$ m. In [30,31], the valve (ball valve) is closed by hand. The valve closure time, measured by the time recorder with an accuracy of 1 ms, is around 0.02 s. The pressure is recorded by means of a measuring system consisting of piezoelectric transducers, a signal amplifier, and a real-time data acquisition system. The steady-state condition in the pipeline is measured with an electromagnetic flow meter. The tests are performed at a constant stream temperature.

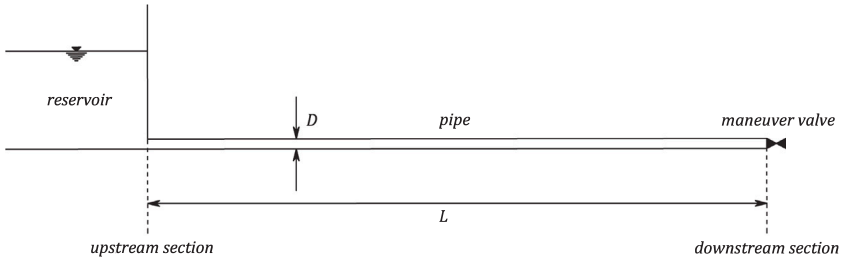

Fig. 2. Sketch of the standard reservoir-pipe-valve system.

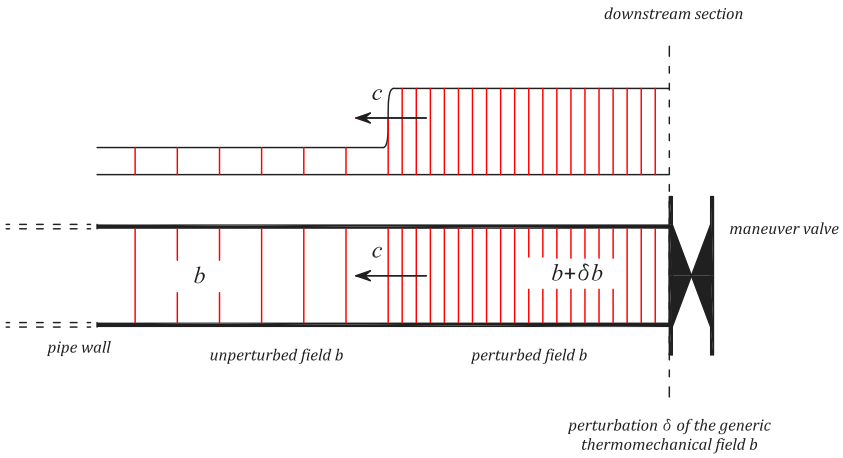

Fig. 3. Sketch of the water hammer wave propagation.

In [32], $L = 98.11$ m, $D = 0.016$ m. A quick-closing spring driven ball valve is installed at the end of the pipe. The records of valve closure show a duration not exceeding 3 ms. The pressure is measured by semiconductor pressure transducers. A turbine flowmeter is used for indirect measurement of average flow velocity in the pipeline. The flowmeter is checked using volumetric method before and after the measurements.

Details of the experimental setup can be found in [15,30–32].

For all test cases, the ratio between the pipe diameter D and the pipe length L is of $O\left(10^{-4}\right)$, very close to that of the classical hydraulic systems, where $\frac{D}{L}$ is typically of $O\left(10^{-4} - 10^{-5}\right)$ [28]. Under these conditions, the hydraulic approximation can be employed [2], i.e., all quantity can assumed to be constant over any pipe cross-section, and the one-dimensional model approximation can be effectively used.

3.2. Analytical solution

The one-dimensional version of Eq. (24) is given as:

$$\frac{\partial^2 \tilde{U}}{\partial \tilde{t}^2} = \frac{\partial^2 \tilde{U}}{\partial \tilde{x}^2} + \frac{1}{\Lambda} \frac{\partial^3 \tilde{U}}{\partial \tilde{x}^2 \partial \tilde{t}}, \tag{28}$$

where x is the spatial coordinate along the pipe axis, with $x = 0$ in the upstream section, $x = L$ in the downstream section; U the cross-section mean velocity (see Fig. 4). The length scale L_0 is set to be equal to pipe length L, $L_0 = L$; thus, $\tilde{x} = \frac{x}{L}$, $\tilde{t} = t\frac{c_0}{L}$, whilst the dimensionless product Λ is expressed as:

$$\Lambda = \frac{c_0 L}{\nu_{d,tur}}. \tag{29}$$

Eq. (28) is defined in the spatial-time dimensionless domain $[0, 1] \times (0, \infty)$. It is appropriate to note that, in the one-dimensional formulation, the continuity and momentum equations read as:

$$\frac{\partial \tilde{p}}{\partial \tilde{t}} + \frac{\partial \tilde{U}}{\partial \tilde{x}} = 0, \tag{30}$$

$$\frac{\partial \tilde{U}}{\partial \tilde{t}} + \frac{\partial \tilde{p}}{\partial \tilde{x}} = \frac{1}{\Lambda} \frac{\partial^2 \tilde{U}}{\partial \tilde{x}^2}, \tag{31}$$

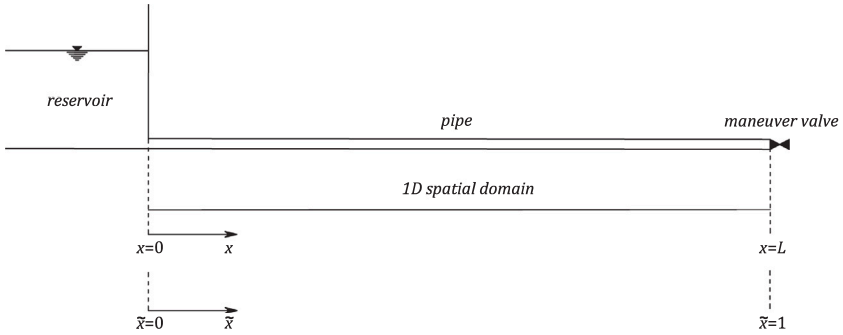

Fig. 4. Sketch of the 1D spatial domain corresponding to the physical domain.

the wave celerity c_0 is given as:

$$c_0 = \sqrt{\frac{\hat{\varepsilon}}{\rho_0}}, \tag{32}$$

where $\hat{\varepsilon}$ is the bulk modulus of elasticity of the liquid-pipe system [34–36], whilst the dissipation function becomes:

$$\tilde{\Phi} = \frac{1}{\Lambda}\left(\frac{\partial \tilde{U}}{\partial \tilde{x}}\right)^2. \tag{33}$$

In agreement with Eq. (32), the bulk modulus $\hat{\varepsilon}$ is assumed to be pressure-independent.

In experimental tests, the reservoir pressure is taken as near-constant, $\tilde{p}\left(0,\tilde{t}\right) \approx constant$, whilst the flow disturbances are identified in the velocity variations due to very rapid closure of the valve. In accordance with the experimental setup, the water hammer wave Eq. (28) is subjected to the initial conditions:

$$\tilde{U} = 1 \quad \text{at} \quad \tilde{t} = 0, \tag{34}$$

$$\frac{\partial \tilde{U}}{\partial \tilde{t}} = 0 \quad \text{at} \quad \tilde{t} = 0, \tag{35}$$

and to the boundary conditions:

$$\frac{\partial \tilde{U}}{\partial \tilde{x}} = 0 \quad \text{at} \quad \tilde{x} = 0, \tag{36}$$

$$\tilde{U} = \mathcal{H}\left(-\tilde{t}\right) \quad \text{at} \quad \tilde{x} = 1, \tag{37}$$

where $\mathcal{H}$ is the Heaviside step function. Eqs. (34)–(35) refer to the steady-state flow conditions; Eq. (36) comes from the constant pressure reservoir condition, in addition with the continuity Eq. (30); Eq. (37) simulates the instantaneous closure of the valve.

The analytical solution of the initial boundary value problem can be expressed as [21,22,37]:

$$\tilde{U} = \mathcal{H}\left(-\tilde{t}\right) + 8\sum_{n=0}^{\infty}(-1)^n \alpha_n \mathrm{e}^{-\frac{\alpha_n^2 \tilde{t}}{2\Lambda}} \cos\left(\alpha_n \tilde{x}\right)\left(\cosh\left(\frac{1}{2}\alpha_n \beta_n \tilde{t}\right) - \frac{\alpha_n}{\Lambda \beta_n}\sinh\left(\frac{1}{2}\alpha_n \beta_n \tilde{t}\right)\right), \tag{38}$$

where:

$$\alpha_n = \frac{\pi}{2}(2n+1), \tag{39}$$

$$\beta_n = \sqrt{\frac{\alpha_n^2}{\Lambda^2} - 4}, \tag{40}$$

with $\frac{\alpha_n^2}{2\Lambda}$ denoting the damping rate of the nth mode, whilst the pressure field at $\tilde{x} = 1$ is given as:

$$\tilde{p} = 1 + 4\sum_{n=0}^{\infty}\frac{1}{\alpha_n \beta_n}\mathrm{e}^{-\frac{\alpha_n^2 \tilde{t}}{2\Lambda}}\sinh\left(\frac{1}{2}\alpha_n \beta_n \tilde{t}\right). \tag{41}$$

Consistent with Eq. (41), or alternatively to Eq. (38), a damped solution with oscillations occurs if $\beta_n < 0$, i.e., if $\Lambda > \frac{\pi}{4}$.

3.3. Comparisons

Eqs. (33), (38), and (41), along with the relationship for Λ (i.e., with relationships for ν_{td} and c_0), could be used to carry out a comprehensive analytical analysis of the dynamic behavior of the water hammer waves. Different formulas to evaluate the wave celerity based on both the bulk modulus of elasticity of the liquid and the mechanical properties of the pipe wall are available in

Table 1
Reference data.

Input data	Test 1 [31]	Test 2 [32]	Test 3 [30]	Test 4 [15]
L_0 (m)	72	98.11	177.4	37.23
D (m)	0.042	0.016	0.036	0.0221
μ_1 (Pa s)	$1 \cdot 10^{-3}$	$9.48 \cdot 10^{-4}$	$1 \cdot 10^{-3}$	$1.13 \cdot 10^{-3}$
U_0 (m/s)	0.405	0.066	0.282	0.1
ρ_0 $(\mathrm{kg/m^3})$	1000	997.65	1000	999.1
p_0 (Pa)	$5.04 \cdot 10^5$	$1.265 \cdot 10^6$	$3.56 \cdot 10^5$	$4.15 \cdot 10^5$
$\mathrm{Re}_{pipe} = \frac{\rho_0 U_0 D}{\mu_1}$	$1.7 \cdot 10^4$	1111	$1.02 \cdot 10^4$	1954
c_{lit} (m/s)	1249	1308	1367	1302
Output data				
c_0 (m/s)	1230	1282	1355	1289
ν_{td} $(\mathrm{m^2/s})$	$2.65 \cdot 10^3$	$3.1 \cdot 10^3$	$4.2 \cdot 10^3$	$7 \cdot 10^2$
$\mathrm{Ma} = \frac{U_0}{c_0}$	$3.3 \cdot 10^{-4}$	$7.8 \cdot 10^{-5}$	$2.1 \cdot 10^{-4}$	$5.1 \cdot 10^{-5}$
$\mathrm{RS}_{tur} = \frac{U_0 L}{\nu_{td}}$	$1.1 \cdot 10^{-2}$	$2.1 \cdot 10^{-3}$	$1.2 \cdot 10^{-2}$	$5.3 \cdot 10^{-3}$
$\Lambda = \frac{c_0 L}{\nu_{d,tur}}$	33.4	40.6	57.2	68.6
c_0/c_{lit}	0.987	0.98	0.99	0.99

Table 2
Initial steady-state conditions [32].

Trial	U_0 (m/s)	p_0 (Pa)	Re_{pipe}
1	0.066	$1.265 \cdot 10^6$	1111
2	0.162	$1.264 \cdot 10^6$	2728
3	0.34	$1.265 \cdot 10^6$	5725
4	0.467	$1.253 \cdot 10^6$	7863
5	0.559	$1.264 \cdot 10^6$	9412
6	0.631	$1.264 \cdot 10^6$	10625
7	0.705	$1.263 \cdot 10^6$	11871
8	0.806	$1.263 \cdot 10^6$	13571
9	0.94	$1.264 \cdot 10^6$	15828

literature [10]; however, small differences can appreciably improve the matching between analytical and experimental data [38]. Due to the lack of knowledge about the turbulent dilatational viscosity, and because of the potential influence of the wave celerity, the values of Λ, i.e., the values of ν_{td} and c_0, are calibrated by fitting the analytical solution to the experimental data. A standard test-and-try procedure is then used.

The experimental parameters setup, the values of the wave celerity c_{lit} predicted by literature formulas, along with a summary of the obtained results are given in Table 1 (as is usual, the Reynolds number for pipe flow, Re_{pipe}, is computed as $\mathrm{Re}_{pipe} = \frac{\rho_0 U_0 D}{\mu_1}$).

As shown in Figs. 5–8, the analytical data are in agreement with the experimental data in terms of peculiar pattern associated with the water hammer waves, such as damping and smoothing, dispersion of wave fronts, and maximum pressure peak.

Fig. 6 shows, in experimental data, an unusual pressure peak at the first cycle that disagrees with the theoretical peak as predicted by the Joukowsky formula [10]; thus, it is not taken into consideration in the comparative analysis. This pressure peak, which, however, does not influence other pressure oscillations, is the result of unwanted mechanical vibrations due to the fast-closing valve; a detailed analysis on this topic can be found in [38,39].

The values of the wave celerity c_{lit}, as reported in [15,30–32], change of a few percentage units with respect to the values c_0.

As the critical Reynolds number $\mathrm{Re}_{pipe,c}$ is about $2 \cdot 10^3$, the initial Reynolds number Re_{pipe} is greater than the critical value in test 1 and test 3; it is lower than the critical value in test 2; it is close to the critical value in test 4. In agreement with the model prediction, initial conditions, related to viscous regime (test 2), fully turbulent regime (test 1 and test 3), or transitional regime (test 4), do not affect the flow behavior. Further confirmation indicating no significant dependence on the Reynolds number comes from the inspection of the nine experimental trials performed in [32], of which the previously used test 2 is part of. Table 2 summarizes the experimental initial steady-state conditions; Fig. 9 shows the experimental data (for a sake of clarity, it should be underlined that the time series are shifted vertically by $3 \cdot 10^6$ Pa, horizontally by 0.05 s). As shown in Fig. 10, these experimental data (for all nine trials) merge in a single curve if plotted in dimensionless form. The same figure shows the comparison between experimental and analytical data. Accordingly, the vorticity field, linked to the initial Reynolds number, has no influence on the propagation of longitudinal waves.

3.4. Entropy production

The dissipative nature of the water hammer waves is highlighted by quantifying the rate of entropy production. This analysis shows the role played by Λ in thermodynamic irreversibilities.

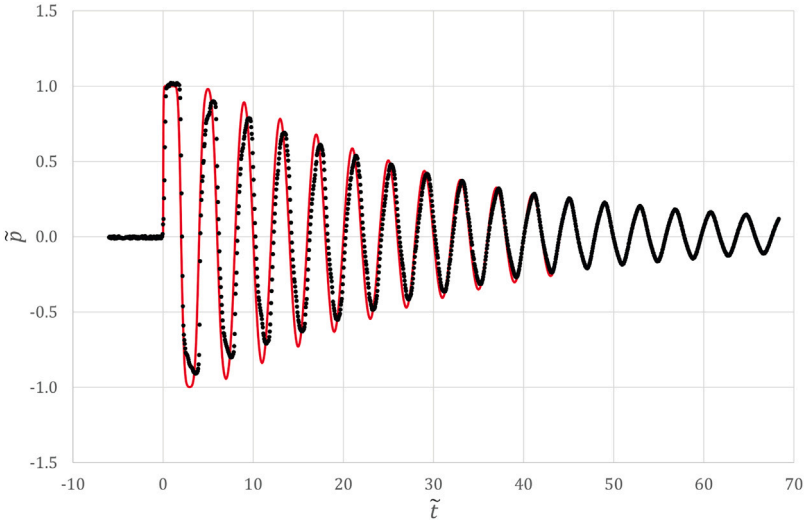

Fig. 5. Test 1. Pressure time-series, where $\tilde{p}$ and $\tilde{t}$ are dimensionless. Continuous line: analytical data; dotted line: experimental data [31]. Parameters: $c_0 = 1230$ m/s; $\nu_{d,tur} = 2.65 \cdot 10^3$ m^2/s; $\Lambda = 33.4$.

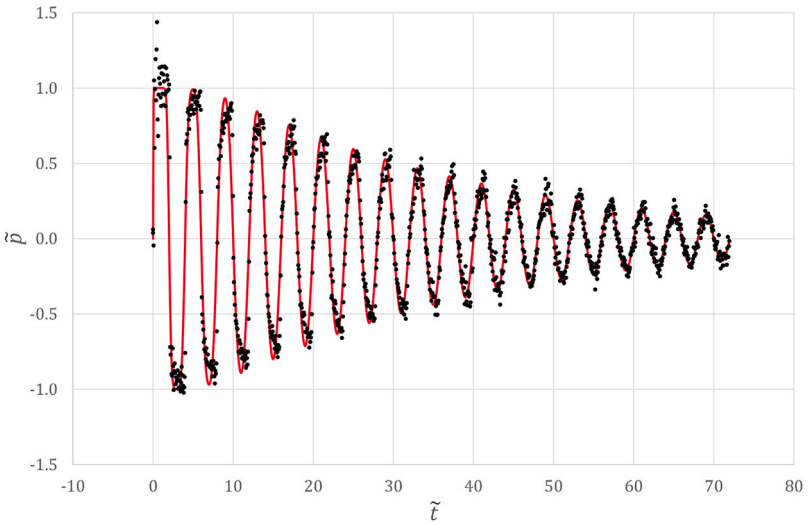

Fig. 6. Test 2. Pressure time-series, where $\tilde{p}$ and $\tilde{t}$ are dimensionless. Continuous line: analytical data; dotted line: experimental data [32]. Parameters: $c_0 = 1282$ m/s; $\nu_{d,tur} = 3.1 \cdot 10^3$ m^2/s; $\Lambda = 40.6$.

The entropy production S is expressed as:

$$\begin{aligned}\tilde{S} &= 2\int_0^1\int_0^{\tilde{t}} \tilde{\Phi}\mathrm{d}\tilde{x}\mathrm{d}\tilde{t} = 2\int_0^1\int_0^{\tilde{t}} \frac{1}{\Lambda}\left(\frac{\partial\tilde{U}}{\partial\tilde{x}}\right)^2 \mathrm{d}\tilde{x}\mathrm{d}\tilde{t} \\ &= 2\sum_{n=0}^{\infty}\frac{1}{\alpha_n^2}\left(1+\mathrm{e}^{-\frac{\alpha_n^2\tilde{t}}{\Lambda}}\left(\frac{4}{\beta_n^2}-\frac{\alpha_n^2}{\Lambda^2\beta_n^2}\cosh\left(\frac{1}{2}\alpha_n\beta_n\tilde{t}\right)-\frac{\alpha_n}{\Lambda\beta_n}\sinh\left(\frac{1}{2}\alpha_n\beta_n\tilde{t}\right)\right)\right),\end{aligned} \tag{42}$$

where $S = \tilde{S}\frac{U_0^2}{2}$.

Fig. 11 shows the evolution of $\tilde{S}$ for each of the test cases. According to the energy conservation principle, for $\tilde{t} \to \infty$, the entropy production equals the initial kinetic energy:

$$\lim_{\tilde{t}\to\infty}\tilde{S} = 2\sum_{n=0}^{\infty}\frac{1}{\alpha_n^2} = \frac{8}{\pi^2}\sum_{n=0}^{\infty}\frac{1}{(2n+1)^2} = 1. \tag{43}$$

As expected, the smaller Λ the shorter the time needed for $\tilde{S}$ to reach the asymptotic value.

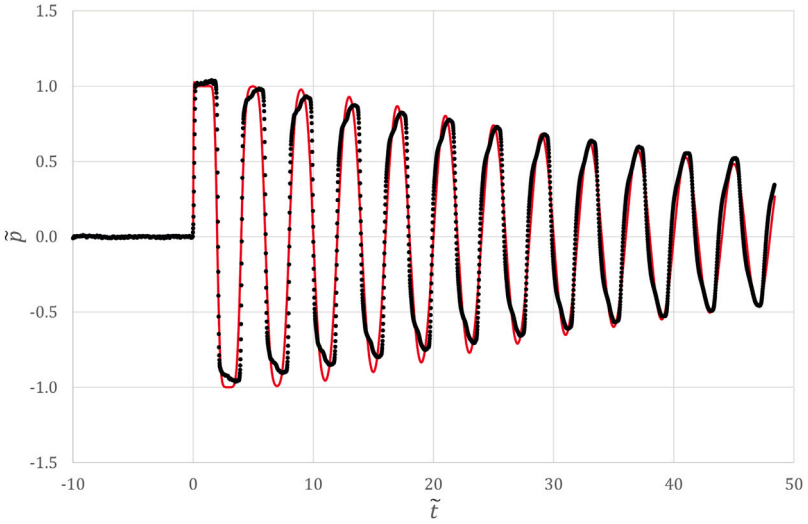

Fig. 7. Test 3. Pressure time-series, where $\tilde{p}$ and $\tilde{t}$ are dimensionless. Continuous line: analytical data; dotted line: experimental data [30]. Parameters: $c_0 = 1355$ m/s; $\nu_{d,tur} = 4.2 \cdot 10^3$ m^2/s; $\Lambda = 57.2$.

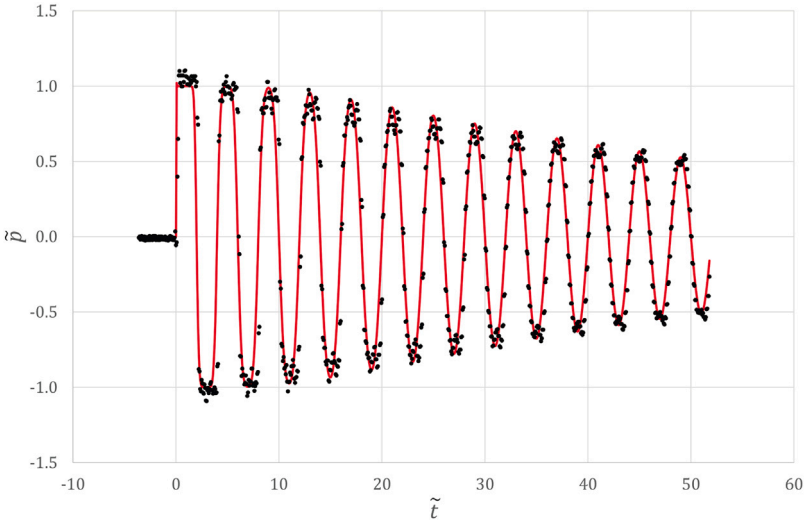

Fig. 8. Test 4. Pressure time-series, where $\tilde{p}$ and $\tilde{t}$ are dimensionless. Continuous line: analytical data; dotted line: experimental data [15]. Parameters: $c_0 = 1289$ m/s; $\nu_{d,tur} = 7 \cdot 10^2$ m^2/s; $\Lambda = 68.6$.

3.5. Damping analysis

The damping analysis is devoted at defining the decrement coefficient $c_{max,k}$ defined as:

$$c_{max,k} = \frac{\tilde{p}_{max,k+1}}{\tilde{p}_{max,k}}, \tag{44}$$

where k is the consecutive pressure amplitude number. To this aim, a numerical analysis is performed to find the roots of equation:

$$\frac{\partial \tilde{p}}{\partial \tilde{t}} = 2 \sum_{n=0}^{\infty} \mathrm{e}^{-\frac{\alpha_n^2 \tilde{t}}{2\Lambda}} \left(\cosh\left(\frac{1}{2}\alpha_n \beta_n \tilde{t}\right) - \frac{\alpha_n}{\Lambda \beta_n} \sinh\left(\frac{1}{2}\alpha_n \beta_n \tilde{t}\right) \right). \tag{45}$$

It should be observed that, according to the model set-up, the water hammer period $\tilde{\tau}_0$ is constant, with $\tilde{\tau}_0 = 4$, as $\tau_0 = 4\frac{L_0}{c_0}$. Thus, the accuracy of the numerical procedure can be also tested comparing $\tilde{\tau}_{num}$ with $\tilde{\tau}_0$, where $\tilde{\tau}_{num}$ is the water hammer period computed numerically. Fig. 12 shows the evolution of the decrement coefficient for each of the test cases. For all test cases, the factor $\frac{\tilde{\tau}_0}{\tilde{\tau}_{num}}$ is found to be very close to unity. In line with model prediction, the damping property is a function of Λ: the smaller Λ the greater the damping.

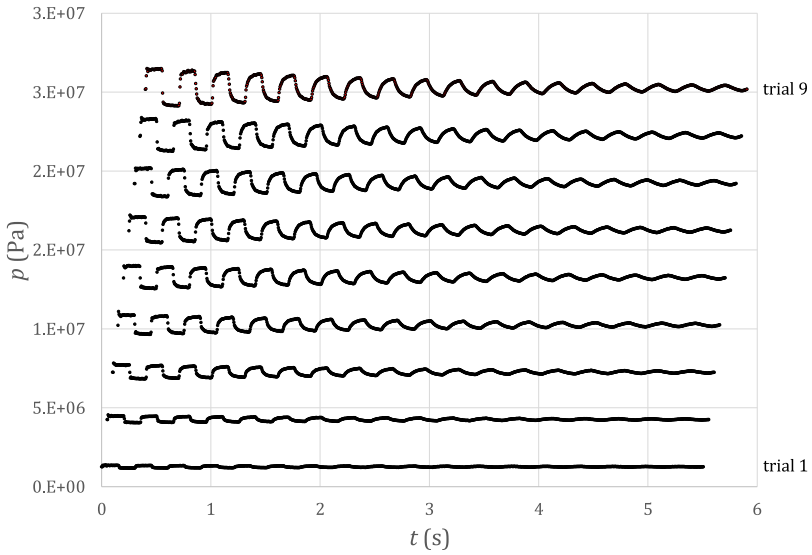

Fig. 9. Experimental data [32].

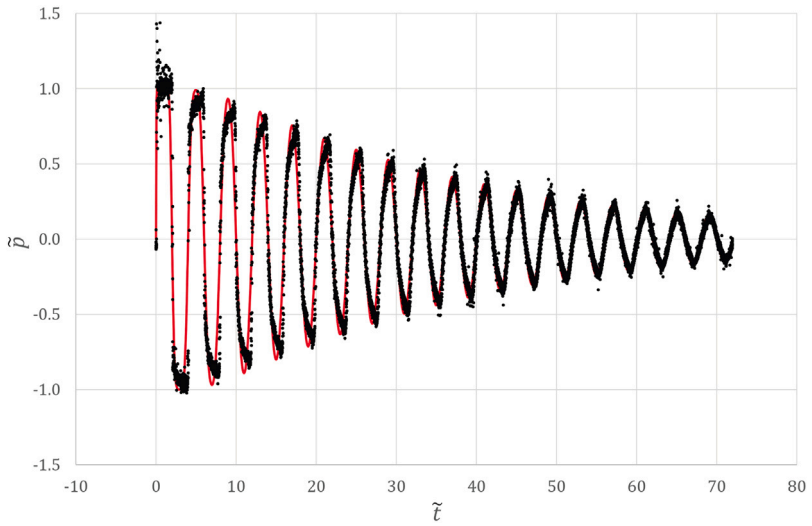

Fig. 10. Pressure time-series, where $\tilde{p}$ and $\tilde{t}$ are dimensionless. Continuous line: analytical data ($\Lambda = 40.6$); dotted line: experimental data [32] (the experimental data are scaled according to the dimensional analysis).

4. Conclusions

Water hammer waves in liquid-filled pipes have been analyzed by means of the linear damped wave equation proposed in [21,22]. This paper has been motivated by both practical relevance and theoretical issues related to this phenomenon. In recalling the model equations, several original aspects have been highlighted. Under the guideline of dimensional analysis, the assumptions made to derive the wave equation have been discussed; among other findings, it has been observed that, in the short time scale, the Reynolds number has an irrelevant role in flow behavior, whilst a single dimensionless number governs the water hammer wave propagation. By using literature experimental data, the wave equation has been tested and validated. Comparisons between analytical and experimental results have shown that the main features of water hammer waves, such as attenuation and dispersion of wave fronts, are well-characterized; prediction of the maximum amplitude of the pressure waves is also achieved. A significant research focus has been directed to proving that the Reynolds number does not affect the water hammer wave propagation. Entropy production and damping properties have been also recognized and discussed. The obtained results support the reliability of the approximations involved in the model equations. In perspective, the wave equation, also due to its simplicity of use, can provide a reference for more complex water hammer models.

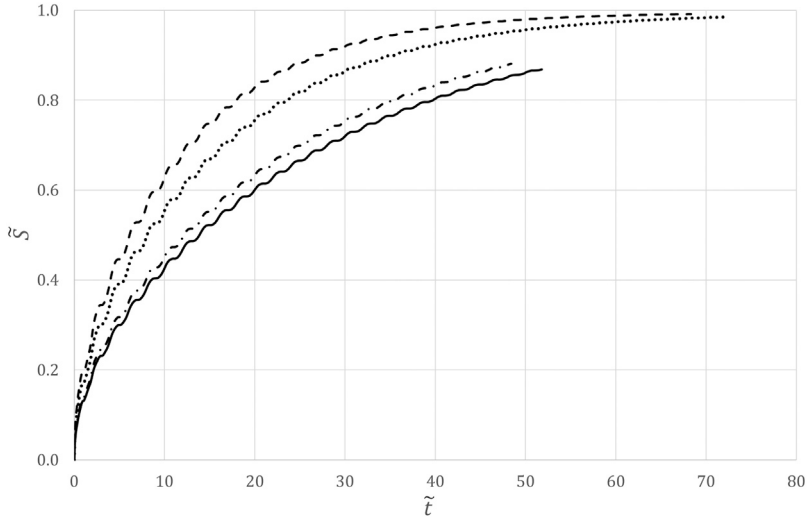

Fig. 11. Entropy production, where $\tilde{S}$ and $\tilde{t}$ are dimensionless. Continuous line: test 4, $\Lambda = 68.6$; dash dot line: test 3, $\Lambda = 57.2$; dotted line: test 2, $\Lambda = 40.6$; dashed line: test 1, $\Lambda = 33.4$.

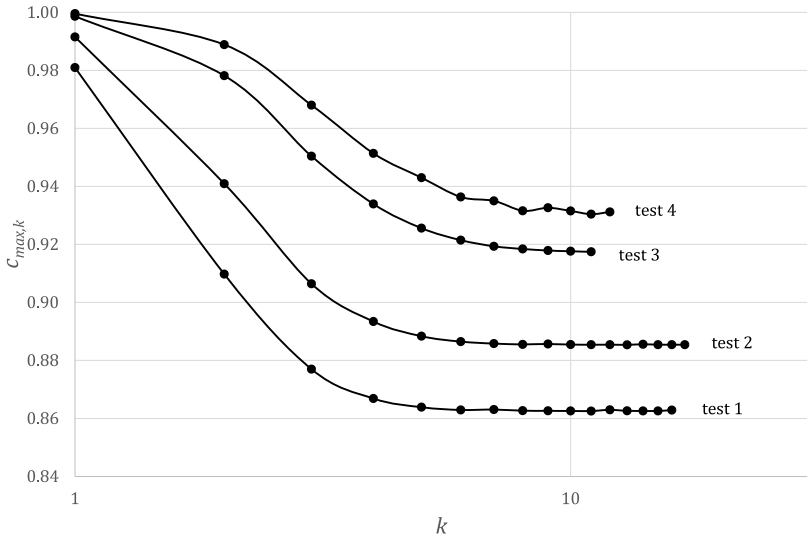

Fig. 12. Evolution of the decrement coefficient (the x-axis is in logarithmic scale). Test 1, $\Lambda = 33.4$; test 2, $\Lambda = 40.6$; test 3, $\Lambda = 57.2$; test 4, $\Lambda = 68.6$.

CRediT authorship contribution statement

Carmine Di Nucci: Writing – review & editing, Writing – original draft, Validation, Supervision, Software, Resources, Methodology, Investigation, Formal analysis, Data curation, Conceptualization. **Kamil Urbanowicz:** Writing – review & editing, Writing – original draft, Validation, Supervision, Software, Resources, Methodology, Investigation, Formal analysis, Data curation, Conceptualization. **Simone Michele:** Writing – review & editing, Writing – original draft, Validation, Supervision, Software, Resources, Methodology, Investigation, Formal analysis, Data curation, Conceptualization. **Daniele Celli:** Writing – review & editing, Writing – original draft, Validation, Supervision, Software, Resources, Methodology, Investigation, Formal analysis, Data curation, Conceptualization. **Davide Pasquali:** Writing – review & editing, Writing – original draft, Validation, Supervision, Software, Resources, Methodology, Investigation, Formal analysis, Data curation, Conceptualization. **Marcello Di Risio:** Writing – review & editing, Writing – original draft, Validation, Supervision, Software, Resources, Methodology, Investigation, Formal analysis, Data curation, Conceptualization.

Declaration of competing interest

All the authors certify that they have NO affiliations with or involvement in any organization or entity with any financial interest (such as honoraria; educational grants; participation in speakers' bureaus; membership, employment, consultancies, stock ownership, or other equity interest; and expert testimony or patent-licensing arrangements), or non-financial interest (such as personal or professional relationships, affiliations, knowledge or beliefs) in the subject matter or materials discussed in this manuscript.

Data availability

Data will be made available on request.

References

[1] P.M. Morse, K.U. Ingard, Theoretical acoustics, Princeton University Press, Princeton, 1986.
[2] L.D. Landau, E.M. Lifshitz, Fluid Mechanics: Landau and Lifshitz: Course of Theoretical Physics, Volume 6, vol. 6, Elsevier, 2013.
[3] W. Hughes, Some aspects of wave propagation in viscous liquids in conduits, Appl. Sci. Res. Sect. A 12 (1963) 119–133.
[4] S. Allam, M. Åbom, Investigation of damping and radiation using full plane wave decomposition in ducts, J. Sound Vib. 292 (3–5) (2006) 519–534.
[5] M. Howe, The damping of sound by wall turbulent shear layers, J. Acoust. Soc. Am. 98 (3) (1995) 1723–1730.
[6] C. Weng, Theoretical and Numerical Studies of Sound Propagation in Low-Mach-Number Duct Flows (Ph.D. thesis), KTH Royal Institute of Technology, 2015.
[7] D. Ronneberger, C. Ahrens, Wall shear stress caused by small amplitude perturbations of turbulent boundary-layer flow: An experimental investigation, J. Fluid Mech. 83 (3) (1977) 433–464.
[8] C. Weng, S. Boij, A. Hanifi, The attenuation of sound by turbulence in internal flows, J. Acoust. Soc. Am. 133 (6) (2013) 3764–3776.
[9] C. Weng, S. Boij, A. Hanifi, Numerical and theoretical investigation of pulsatile turbulent channel flows, J. Fluid Mech. 792 (2016) 98–133.
[10] M.S. Ghidaoui, M. Zhao, D.A. McInnis, D.H. Axworthy, A review of water hammer theory and practice, Appl. Mech. Rev. 58 (1) (2005) 49–76.
[11] A. Tijsseling, Fluid-structure interaction in liquid-filled pipe systems: A review, J. Fluids Struct. 10 (2) (1996) 109–146.
[12] S. Li, B.W. Karney, G. Liu, FSI research in pipeline systems–a review of the literature, J. Fluids Struct. 57 (2015) 277–297.
[13] R. Puust, Z. Kapelan, D. Savic, T. Koppel, A review of methods for leakage management in pipe networks, Urban Water J. 7 (1) (2010) 25–45.
[14] W. Zielke, Frequency-dependent friction in transient pipe flow, J. Basic Eng. 90 (1968) 109–115.
[15] A. Bergant, A. Ross Simpson, J. Vìtkovsk, Developments in unsteady pipe flow friction modelling, J. Hydraul. Res. 39 (3) (2001) 249–257.
[16] K. Urbanowicz, Fast and accurate modelling of frictional transient pipe flow, ZAMM- J. Appl. Math. Mech./ Z. Angew. Math. Mech. 98 (5) (2018) 802–823.
[17] K. Urbanowicz, A. Bergant, M. Stosiak, M. Karpenko, M. Bogdevičius, Developments in analytical wall shear stress modelling for water hammer phenomena, J. Sound Vib. 562 (2023) 117848.
[18] K. Urbanowicz, H. Jing, A. Bergant, M. Stosiak, M. Lubecki, Progress in analytical modeling of water hammer, J. Fluids Eng. 145 (8) (2023) 081203.
[19] C. Di Nucci, D. Pasquali, D. Celli, A. Pasculli, P. Fischione, M. Di Risio, Turbulent bulk viscosity, Eur. J. Mech. B Fluids 84 (2020) 446–454.
[20] C. Di Nucci, D. Celli, D. Pasquali, M. Di Risio, New dimensionless number for the transition from viscous to turbulent flow, Fluids 7 (6) (2022) 202.
[21] C. Di Nucci, S. Michele, M. Di Risio, Decomposition of the mechanical stress tensor: From the compressible Navier–Stokes equation to a turbulent potential flow model, Acta Mech. (2024a) 1–18.
[22] C. Di Nucci, S. Michele, M. Di Risio, Modeling of low mach number unsteady turbulent pipe flows, Meccanica 59 (2024b) 717–728.
[23] G. Tomassetti, An interpretation of Temam's extra force in the quasi-incompressible Navier–Stokes system, Appl. Eng. Sci. 5 (2021) 100028.
[24] J.-Z. Wu, H.-Y. Ma, M.-D. Zhou, Vortical Flows, vol. 28, Springer, Berlin, 2015.
[25] K. Rajagopal, Remarks on the notion of "pressure", Int. J. Non-Linear Mech. 71 (2015) 165–172.
[26] J. Spurk, N. Aksel, Fluid Mechanics, Springer Science & Business Media, Berlin, 2007.
[27] T.-Y. Kim, J. Dolbow, E. Fried, A numerical method for a second-gradient theory of incompressible fluid flow, J. Comput. Phys. 223 (2) (2007) 551–570.
[28] R.P. Benedict, Fundamentals of Pipe Flow, Wiley, New York, 1980.
[29] M. Galimzyanov, U. Agisheva, Propagation of a pressure wave in a tube filled with liquid containing of a bubble cluster in the form of a hollow cylinder, Fluid Dyn. 58 (8) (2023) 1495–1501.
[30] R. Szymkiewicz, M. Mitosek, Alternative convolution approach to friction in unsteady pipe flow, J. Fluids Eng. 136 (1) (2014) 011202.
[31] M. Mitosek, R. Szymkiewicz, Wave damping and smoothing in the unsteady pipe flow, J. Hydraul. Eng. 138 (7) (2012) 619–628.
[32] A. Adamkowski, M. Lewandowski, Experimental examination of unsteady friction models for transient pipe flow simulation, J. Fluids Eng. 128 (6) (2006) 1351–1363.
[33] M. Galimzyanov, I. Gimaltdinov, V.S. Shagapov, Two-dimensional pressure waves in a fluid with bubbles, Fluid Dyn. 37 (2) (2002) 294–301.
[34] C. Di Nucci, M. Petrilli, A. Russo Spena, Unsteady friction and visco-elasticity in pipe fluid transients, J. Hydraul. Res. 49 (3) (2011) 398–401.
[35] C. Di Nucci, A. Russo Spena, On the propagation of one-dimensional acoustic waves in liquids, Meccanica 48 (2013) 15–21.
[36] C. Di Nucci, A. Russo Spena, On transient liquid flow, Meccanica 51 (9) (2016) 2135–2143.
[37] C. Mei, Y. Li, S. Michele, P. Sammarco, P. McBeth, Anchoring and migration of balloon in REBOA, J. Fluid Mech. 927 (2021) A20.
[38] K. Urbanowicz, A. Bergant, M. Stosiak, A. Deptuła, M. Karpenko, M. Kubrak, A. Kodura, Water hammer simulation using simplified convolution-based unsteady friction model, Water 14 (19) (2022) 3151.
[39] A. Adamkowski, S. Henclik, W. Janicki, M. Lewandowski, The influence of pipeline supports stiffness onto the water hammer run, Eur. J. Mech. B Fluids 61 (2017) 297–303.